1D studies of long-legged divertor following from benchmark of SOLF1D and SOLPS codes

E Havlíčková[1], W Fundamenski, F Subba, D Coster, M Wischmeier, G Fishpool

[1] EURATOM/CCFE Fusion Association, Culham Science Centre, Abingdon, Oxon, OX14 3DB, United Kingdom.

E-mail: eva.havlickova@ccfe.ac.uk

Abstract. A 1D code modelling SOL transport parallel to the magnetic field (SOLF1D) is benchmarked with two 2D simulations of MAST-U SOL of different collisionalities performed in SOLPS/EIRENE. Based on this comparison, SOLF1D is then used to model the effects of divertor leg stretching in 1D, in support of the new Super-X divertor on MAST. The aim is to separate magnetic flux expansion from volumetric sources due to recycling neutrals by stretching the divertor leg either vertically ($\nabla B_{\|} = 0$ in the divertor) or radially ($B \propto 1/R$).

1. Introduction

The divertor geometry is one of the important aspects influencing the SOL performance. A reduction of plasma temperatures in the divertor and energy fluxes to the targets can be gained by stretching the divertor leg to larger radius via effects of magnetic flux expansion and longer connection length $L_{\|}$, and via effects of plasma-neutral interaction and radiation.

In support of the new Super-X divertor on MAST [1], numerical investigations of effects associated with long-legged divertor geometry are undertaken using SOL transport codes. In this paper, 1D studies performed with SOLF1D code are presented, while 2D effects have been simulated by SOLPS/EIRENE and will be presented in a separate paper. The 1D model enables to separate effects of magnetic flux expansion induced by $\nabla_{\|}B$ from cooling by plasma-neutral interaction (both functions of the divertor length) by the possibility of prescribing any parallel/radial dependence of the magnetic field. Such approach is flexible enough to run large number of scans compared to robust 2D codes where the preparation of a simulation for a new geometry is always time-demanding. However, 1D approach is limited in terms of the determination of sources/sinks in the divertor due to atomic processes, which are governed by 2D transport of neutral species in the divertor. 1D results are therefore related to SOLPS/EIRENE simulations perfomed for two configurations with different divertor leg lengths, which provide a baseline for the scaling of upstream cross-field transport and recycling divertor sources with increasing $L_{\|}$. Alternatively, a 1D neutral model in SOLF1D can be used to describe recycling sources self-consistently, however still excluding 2D processes.

In order to link the 1D and 2D codes, plasma transport model in SOLF1D is first benchmarked with SOLPS5.0 model, section 3. The code comparison is discussed in detail as several discrepancies have been identified. In the following section, 1D effects of the long-legged divertor are discussed based on SOLF1D results. Finally, the first complete documentation for the SOLF1D code is provided in appendix.

2. Model description

2.1. SOLF1D model for MAST

SOLF1D is a one-dimensional code solving plasma transport equations along the magnetic field line in the SOL between two targets. Braginskii-like equations in SOLF1D defined in [2] have been generalized to take into account parallel gradient of the magnetic field $\partial B/\partial s$, while it is assumed that the magnetic field does not change in time $\partial B/\partial t = 0$. This is done in conformity with generalized fluid equations for parallel transport documented in [3]-[4] or [5]. Here, a brief description of the model needed for the code benchmark is provided, while more complete documentation of the SOLF1D model can be found in appendix.

The set of equations solved in the code includes the continuity and momentum

equations for plasma density $n_\mathrm{e} = n_\mathrm{i} = n$ and parallel ion velocity $u_\parallel$ and energy equations for electrons and ions

$$\frac{\partial n}{\partial t} + B\frac{\partial}{\partial s_\parallel}\left(\frac{nu_\parallel}{B}\right) = S^n, \tag{1}$$

$$\frac{\partial}{\partial t}(m_\mathrm{i} n u_\parallel) + B\frac{\partial}{\partial s_\parallel}\left(\frac{m_\mathrm{i} n u_\parallel^2}{B}\right) + B^{\frac{3}{2}}\frac{\partial}{\partial s_\parallel}\left(B^{-\frac{3}{2}}\delta p_\mathrm{i}\right) = -\frac{\partial p_\mathrm{i}}{\partial s_\parallel} + enE_\parallel + R_{\parallel,\mathrm{i}} + m_\mathrm{i} S^u_\parallel, \tag{2}$$

$$\frac{\partial}{\partial t}\left(\frac{3}{2}nkT_\mathrm{e}\right) + B\frac{\partial}{\partial s_\parallel}\left[\frac{1}{B}\left(\frac{5}{2}nkT_\mathrm{e}u_\parallel + q_{\parallel,\mathrm{e}}\right)\right] = -enu_\parallel E_\parallel + u_\parallel R_{\parallel,\mathrm{e}} + Q_\mathrm{e} + S^E_\mathrm{e}, \tag{3}$$

$$\frac{\partial}{\partial t}\left(\frac{3}{2}nkT_\mathrm{i} + \frac{1}{2}m_\mathrm{i} n u_\parallel^2\right) + B\frac{\partial}{\partial s_\parallel}\left[\frac{1}{B}\left(\frac{5}{2}nkT_\mathrm{i}u_\parallel + \frac{1}{2}m_\mathrm{i} n u_\parallel^3 + q_{\parallel,\mathrm{i}} + u_\parallel \delta p_\mathrm{i}\right)\right] = \tag{4}$$
$$enu_\parallel E_\parallel + u_\parallel R_{\parallel,\mathrm{i}} + Q_\mathrm{i} + S^E_\mathrm{i}.$$

Zero net parallel current is assumed $j_\parallel = 0$ ($u_{\parallel,\mathrm{e}} = u_{\parallel,\mathrm{i}}$) together with the generalized Ohm's law for electron momentum $enE_\parallel = -\partial p_\mathrm{e}/\partial s_\parallel + R_{\parallel,\mathrm{e}}$. S^n, S^u, S^E_e and S^E_i are sources due to collisions with neutrals and cross-field transport sources. Q_e and Q_i is the heating due to electron-ion collisions, $q_{\parallel,\mathrm{e}} = -\kappa_e \partial(kT_\mathrm{e})/\partial s_\parallel$ and $q_{\parallel,\mathrm{i}} = -\kappa_i \partial(kT_\mathrm{i})/\partial s_\parallel$ are the electron and ion heat fluxes, p_e and p_i is the electron and ion static pressure and $\delta p_\mathrm{i} = -\eta_\parallel B^{-1/2}\partial/\partial s_\parallel (B^{1/2}u_\parallel)$ reflects the anisotropic part of the pressure tensor for ions (electrons are assumed Maxwellian $\delta p_\mathrm{e} = 0$).

Boundary conditions at the targets are based on the sheath theory and include the Bohm criterion for the ion speed $u_\parallel = c_\mathrm{s}$ and energy fluxes controlled by sheath heat transmission factors $Q_{\parallel,\mathrm{e}} = \delta_\mathrm{e} nkT_\mathrm{e} c_\mathrm{s}$ and $Q_{\parallel,\mathrm{i}} = \delta_\mathrm{i} nkT_\mathrm{i} c_\mathrm{s}$. $Q_\parallel$ denotes the total energy flux, $Q_{\parallel,\mathrm{e}} = 5/2 nkT_\mathrm{e}u_\parallel + q_{\parallel,\mathrm{e}}$ and $Q_{\parallel,\mathrm{i}} = 5/2 nkT_\mathrm{i}u_\parallel + 1/2 m_\mathrm{i} n u_\parallel^3 + q_{\parallel,\mathrm{i}} + u_\parallel \delta p_\mathrm{i}$. The sound speed is defined as $c_\mathrm{s} = \sqrt{k(T_\mathrm{e} + T_\mathrm{i})/m_\mathrm{i}}$. The sheath heat transmission coefficients are fixed to constant values of $\delta_\mathrm{e} = 5.0$ and $\delta_\mathrm{i} = 3.5$. The density at the target is obtained by extrapolation.

2.2. SOLPS equations and their reduction to 1D

The SOLPS model is based on Braginskii equation [6] solved in the poloidal geometry, i.e. assuming toroidal symmetry. The conservation equations are written in curvilinear coordinates coinciding with the magnetic topology. The equations solved in SOLPS are documented in [6]. Here, SOLPS5.0 version without drifts is used. We also assume that $j_\parallel = 0$ and the potential equation is not followed. Parallel transport is described by Braginskii model with the use of viscous and heat flux limiters. Note that the change from Balescu to Braginskii transport coefficients and setting $j_\parallel = 0$ has no visible effect on solution for the MAST-U case investigated here, while it assures consistency with the 1D model. In addition, there is no impurity present in the simulation which results in increased plasma temperature at the outer target by 30% in comparison with a simulation including C sputtering. SOLPS equations in [6] can be simplified into the

following form

$$\frac{\partial n}{\partial t}+\frac{1}{\sqrt{g}}\frac{\partial}{\partial x}\left(\frac{\sqrt{g}}{h_x}nu_x\right)+\frac{1}{\sqrt{g}}\frac{\partial}{\partial y}\left(\frac{\sqrt{g}}{h_y}nu_y\right)=S^{(n)} \tag{5}$$

with $u_x = b_x u_\parallel + b_z u_\perp$ and anomalous radial transport reflected in the radial velocity as $u_y = -(D^n/nh_y)\partial n/\partial y$, $b_z u_\perp = -(D^n/nh_x)\partial n/\partial x$,

$$\begin{aligned} m_\mathrm{i}\left[\frac{\partial nu_\parallel}{\partial t}+\frac{1}{h_z\sqrt{g}}\frac{\partial}{\partial x}\left(\frac{h_z\sqrt{g}}{h_x}nu_xu_\parallel\right)+\frac{1}{h_z\sqrt{g}}\frac{\partial}{\partial y}\left(\frac{h_z\sqrt{g}}{h_y}nu_yu_\parallel\right)\right] \\ -\frac{4}{3}b_xB^{\frac{3}{2}}\frac{\partial}{h_x\partial x}\left(\frac{\eta_0 b_x}{B^2}\frac{\partial B^{\frac{1}{2}}u_\parallel}{h_x\partial x}\right)-B^{\frac{3}{2}}b_x\frac{\partial}{h_x\partial x}\left(\frac{b_x}{\nu_\mathrm{ii}B^2}\frac{\partial B^{\frac{1}{2}}q_{\parallel,\mathrm{i}}}{h_x\partial x}\right)= \\ -\frac{b_x}{h_x}\frac{\partial p_\mathrm{i}}{\partial x}-b_x\frac{en}{h_x}\frac{\partial\phi}{\partial x}+R_{\parallel,\mathrm{i}}+S_\parallel^{(u)} \end{aligned} \tag{6}$$

with additional parallel viscosity driven by ion heat flux $q_{\parallel,\mathrm{i}} = -\kappa_{\parallel,\mathrm{i}} b_x \partial T_\mathrm{i}/h_x\partial x$ which is not included in the standard Braginskii model,

$$\frac{3}{2}\frac{\partial nkT_\mathrm{e}}{\partial t}+\frac{1}{\sqrt{g}}\frac{\partial}{\partial x}\left(\frac{\sqrt{g}}{h_x}q_{x,\mathrm{e}}\right)+\frac{1}{\sqrt{g}}\frac{\partial}{\partial y}\left(\frac{\sqrt{g}}{h_y}q_{y,\mathrm{e}}\right)+\frac{nkT_\mathrm{e}}{\sqrt{g}}\frac{\partial}{\partial x}\left(\frac{\sqrt{g}}{h_x}b_xu_\parallel\right)=Q_\mathrm{e}+S_\mathrm{e}^{(E)}, \tag{7}$$

$$\begin{aligned} q_{x,\mathrm{e}} &= \frac{3}{2}nkT_\mathrm{e}b_xu_\parallel-\kappa_{\parallel,\mathrm{e}}\frac{b_x^2}{h_x}\frac{\partial kT_\mathrm{e}}{\partial x}-\frac{5}{2}nkT_\mathrm{e}b_zD_\mathrm{an}\frac{1}{h_xn}\frac{\partial n}{\partial x}, \\ q_{y,\mathrm{e}} &= -\frac{5}{2}nkT_\mathrm{e}D_\mathrm{an}\frac{1}{h_yn}\frac{\partial n}{\partial y}, \end{aligned}$$

$$\frac{3}{2}\frac{\partial nkT_\mathrm{i}}{\partial t}+\frac{1}{\sqrt{g}}\frac{\partial}{\partial x}\left(\frac{\sqrt{g}}{h_x}q_{x,\mathrm{i}}\right)+\frac{1}{\sqrt{g}}\frac{\partial}{\partial y}\left(\frac{\sqrt{g}}{h_y}q_{y,\mathrm{i}}\right)+\frac{nkT_\mathrm{i}}{\sqrt{g}}\frac{\partial}{\partial x}\left(\frac{\sqrt{g}}{h_x}b_xu_\parallel\right)=Q_\mathrm{vis}+Q_\mathrm{i}+S_\mathrm{i}^{(E)}, \tag{8}$$

$$\begin{aligned} q_{x,\mathrm{i}} &= \frac{3}{2}nkT_\mathrm{i}b_xu_\parallel-\kappa_{\parallel,\mathrm{i}}\frac{b_x^2}{h_x}\frac{\partial kT_\mathrm{i}}{\partial x}-\frac{5}{2}nkT_\mathrm{i}b_zD_\mathrm{an}\frac{1}{h_xn}\frac{\partial n}{\partial x}, \\ q_{y,\mathrm{i}} &= -\frac{5}{2}nkT_\mathrm{i}D_\mathrm{an}\frac{1}{h_yn}\frac{\partial n}{\partial y}, \\ Q_\mathrm{vis} &= \frac{\eta_0}{3}\left(\frac{2b_x}{\sqrt{B}}\frac{\partial u_\parallel\sqrt{B}}{h_x\partial x}\right)^2. \end{aligned}$$

It can be shown that Eqs. (5)-(8) reduce into 1D equations similar to Eqs. (1)-(4). In the code, the equations are discretized using the finite volume method. For example, the finite volume form of the continuity equation (5) assuming steady state is

$$\Delta F_x^n+\Delta F_y^n=S^{(n)}V \tag{9}$$

where on the left side, we sum the particle fluxes F_x^n and F_y^n entering and leaving the cell across the cell boundaries, and the right side represents the total particle net source in s^{-1} on the cell with the volume V.

The poloidal flux F_x^n across the cell face is calculated as $F_x^n = nu_\parallel AB_x/B$, $A = 2\pi Rh$ is the radial area of the cell perpendicular to the poloidal direction with the radial size of the cell h across the flux tube. Because SOLPS does not use a staggered

grid for all flow variables, the Rhie-Chow interpolation method is employed to take the cell-centre values of the parallel velocity $u_\parallel$ on the cell faces where fluxes are calculated. The cell volume is defined as $V = 2\pi Rh\Delta x$. Following from Eq. (9), the poloidal part of the flux divergence can be translated as

$$\frac{\Delta F_x^n}{V} = \frac{1}{A}\frac{\Delta\left(nu_\parallel A\frac{B_x}{B}\right)}{\Delta x} = \frac{1}{Rh}\frac{\Delta\left(nu_\parallel Rh\frac{B_x}{B}\right)}{\Delta x}. \tag{10}$$

Using (i) $B_z \propto 1/R$ and (ii) $hB_x/B_z = \text{const}$ along the flux tube, and replacing Δx by $(B_x/B)\Delta s_\parallel$, this further yields

$$\frac{\Delta F_x^n}{V} = \frac{1}{Rh}\frac{\Delta\left(nu_\parallel Rh\frac{B_x}{B}\right)}{\Delta x} = B_x\frac{\Delta\left(\frac{nu_\parallel}{B}\right)}{\Delta x} = B\frac{\Delta\left(\frac{nu_\parallel}{B}\right)}{\Delta s_\parallel}, \tag{11}$$

equivalent to the divergence term of the 1D equation

$$B\frac{\Delta\left(\frac{nu_\parallel}{B}\right)}{\Delta s_\parallel} = S^n \tag{12}$$

consistent with the one solved in SOLF1D, Eq. (1). The radial part of the flux divergence $\Delta F_y^n/V_{\text{cell}}$ from Eq. (9) appears as a source term in the equation parallel to the magnetic field (12), $S^n = S^{(n)} - \Delta F_y^n/V$.

Boundary conditions in SOLPS for quantities at the target are not exactly identical to those in SOLF1D. In SOLPS, the density is calculated assuming zero gradient at the target and the parallel ion velocity is set to the sound speed $u_\parallel = c_\text{s}$. The target energy fluxes are prescribed as $Q^{\text{in}}_{\parallel,\text{e}} = 3/2nkT_\text{e}u_\parallel + q_{\parallel,\text{e}} = \gamma_\text{e}nkT_\text{e}c_\text{s}$ and $Q^{\text{in}}_{\parallel,\text{i}} = 3/2nkT_\text{i}u_\parallel + q_{\parallel,\text{i}} = \gamma_\text{i}nkT_\text{i}c_\text{s}$ with $\gamma_\text{e} = 4.0$ and $\gamma_\text{i} = 2.5$ (SOLPS solves the internal energy equation instead of the typical conservative form of energy balance), i.e. the ion kinetic and viscous parts of the energy flux are not included in the boundary condition.

3. Benchmark of codes

For benchmarking the codes, two converged SOLPS solutions were selected. Both are MAST-U cases, H-mode plasma, in CDN magnetic configuration, the first one for SXD geometry, the second one for the conventional divertor geometry (Fig. 1 left). These cases have been studied in [13]. The power to the SOL is $P_\text{inp} = 1.7MW$ and the density at the core boundary is $n_\text{core} = 2.8 \times 10^{19}$ m^{-3}. A flux tube used for the comparison is close to the separatrix and it is the flux tube with maximum energy flux at the target. On the right side, the magnetic field along this flux tube between top and bottom targets is shown, with larger drop in SXD as expected from the extension of the divertor to larger radius.

Sources from EIRENE due to plasma-neutral collisions and sources from SOLPS due to radial transport are used as an input for SOLF1D, together with the magnetic field variation along the flux tube. The sources are displayed in Figs. 2-3. The energy sources are dominated by the radial transport in the upstream SOL and around X points. The contribution from the electron cooling due to plasma-neutral interaction

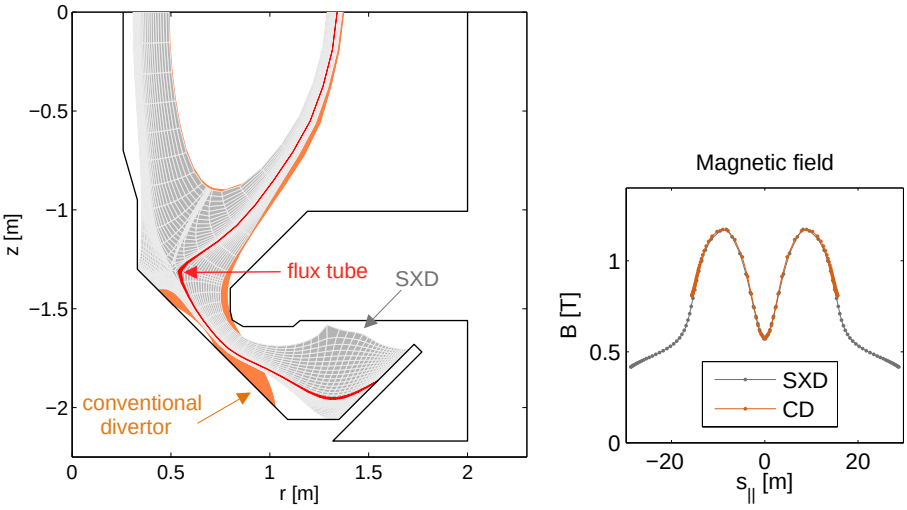

Figure 1. On the left, two divertor geometries used for benchmarking the codes – conventional divertor and SXD. The grid is top/bottom symmetric and the flux tube selected for benchmarking, shown in red, is located at the strike point at the outboard side between top and bottom targets. On the right, the magnetic field along the flux tube is shown for the two divertor configurations.

close to the targets is small compared to the radial transport, but it is stronger in the SXD case than in the CD case. The particle sources are dominated by recycling at the targets, which is again amplified in the SXD case (larger divertor volume, closed divertor, smaller temperatures).

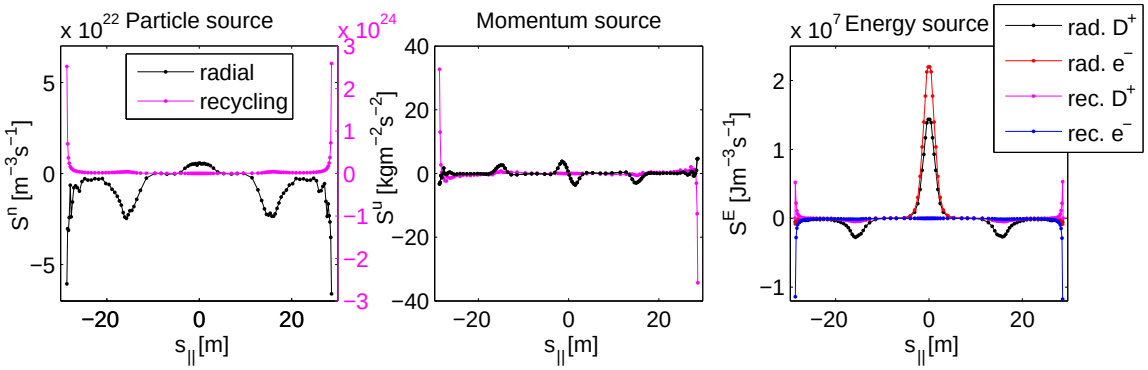

Figure 2. SXD geometry – sources of particles, momentum and energy along a flux tube located close to the separatrix between the top and bottom outer targets. Two types of sources are shown – sources due to transport radially across the flux tube and sources due to recycling calculated in EIRENE.

Solutions of SOLF1D and SOLPS on a flux tube (from Fig. 1) in the SXD geometry (using sources from Fig. 2) are compared in Fig. 4, showing very good agreement between the codes. Similar level of agreement has been achieved also for the conventional divertor geometry in the most of the SOL, apart from flux tubes located very close to the separatrix, to which further attention is devoted in order to identify the origin of

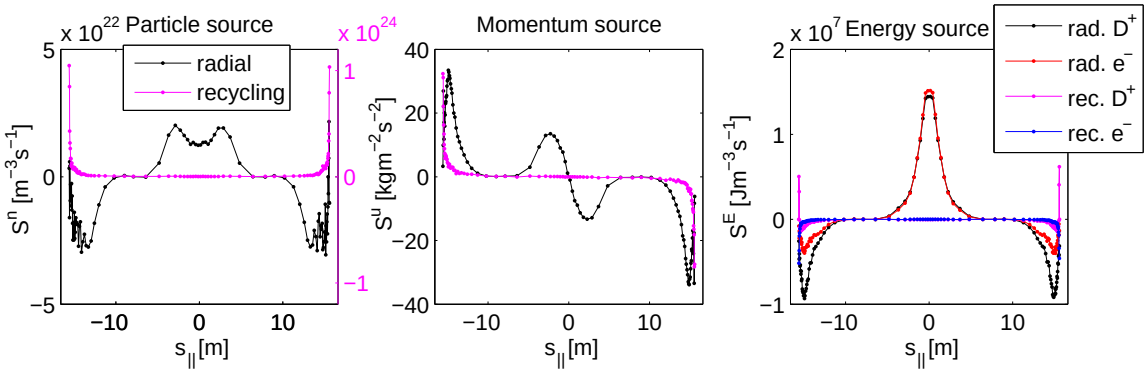

Figure 3. Conventional divertor geometry – sources of particles, momentum and energy along a flux tube.

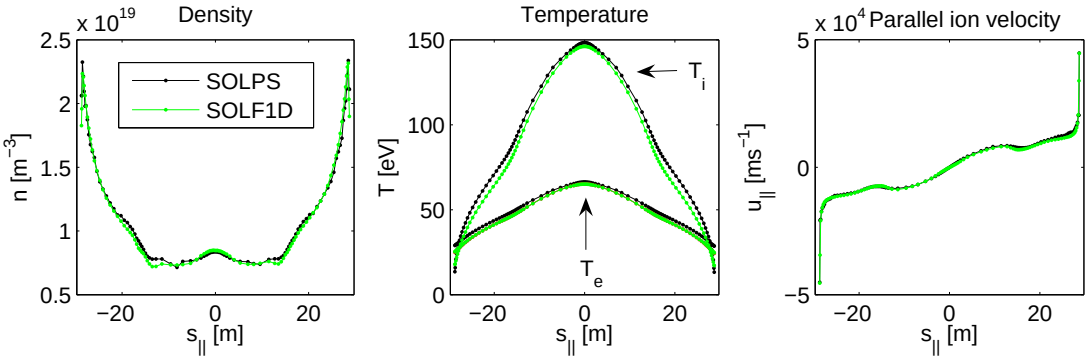

Figure 4. A flux tube in the SXD grid – comparison of SOLF1D and SOLPS solutions.

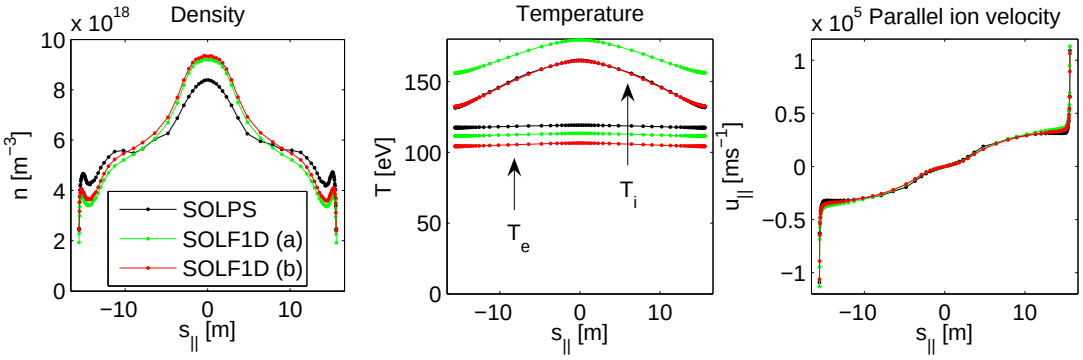

Figure 5. A flux tube in the CD grid – comparison of SOLF1D and SOLPS solutions.

the mismatch. An example of the least satisfactory result (using sources from Fig. 3) is presented in Fig. 5. Discrepancies up to 15% are observed, with the largest disagreement in the ion temperatures (compare black versus green). The main reason for this disagreement is different boundary condition used in the codes for T_i, see sections 2.1-2.2. If the boundary condition in SOLF1D is identical with the one used in SOLPS, perfect match of the ion temperatures is obtained (compare black versus red), however a disagreement in n and T_e is still present.

Several checks were carried out to identify the cause of the disagreement, including

a test of the grid resolution (SOLF1D solutions in Figs. 4-5 are spatially converged), a check of boundary conditions, a comparison for simplified cases reducing physics of the model, a test of inaccuracy due to 2D numerical discretization in SOLPS. Fig. 6 shows plasma quantities at the target with different boundary conditions used in the codes. For further comparison, boundary conditions in SOLF1D are fixed to those in SOLPS.

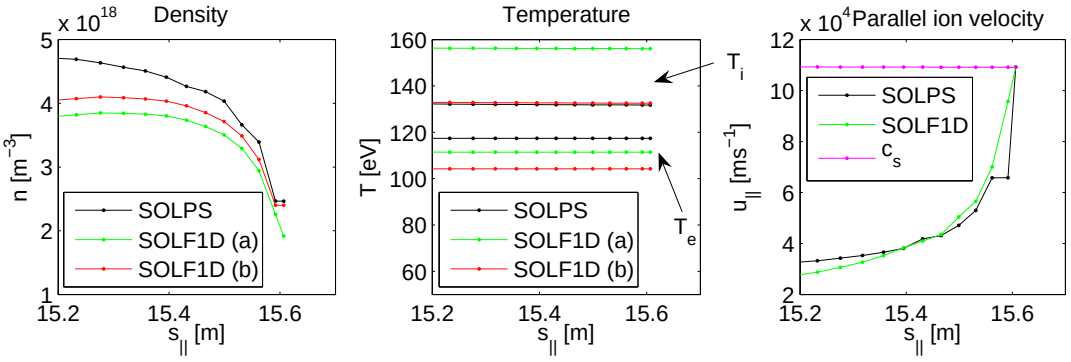

Figure 6. Boundary condition in the codes. (i) Plasma density close to the target from SOLPS (black), SOLF1D using standard extrapolation boundary condition (case a) and SOLF1D using zero gradient boundary condition (case b). (ii) Plasma temperatures close to the target shown as a comparison of SOLPS solution versus SOLF1D result using standard SOLF1D boundary conditions (case a) or using boundary conditions identical to SOLPS (case b). (iii) Parallel ion velocity at the target follows the same boundary condition, $u_{\|} = c_s$, in both codes. The solution is shown for the same temperature in the codes.

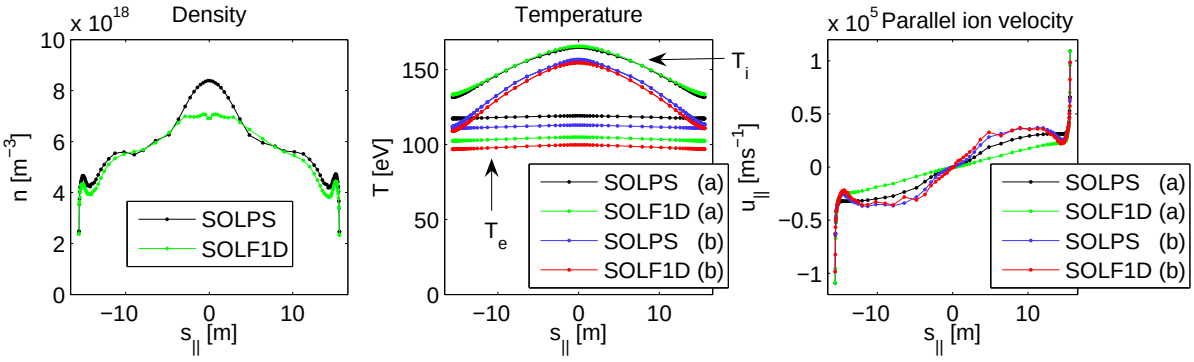

Figure 7. A flux tube in the CD grid – comparison of SOLF1D and SOLPS solutions for a reduced model. (i) Benchmark of density solvers only (left). (ii) Benchmark of temperature solvers only (middle) – (a) full model, (b) reduced model neglecting viscous heating and electron-ion equipartition. (iii) Benchmark of velocity solvers only (right) – (a) full model, (b) reduced model neglecting viscous fluxes.

For the same case, Fig. 7 shows the best agreement we can achieve between the codes. Here, we use the same boundary conditions in SOLF1D as in SOLPS for all quantities and we reduce the equations even further to assure that there are no differences between the models. We test the continuity, momentum and energy solvers

one by one, i.e. the density shown on the left is obtained with fixing the velocity and temperature in SOLF1D to SOLPS profiles so that only the continuity solvers are tested, and similarly the temperature and velocity profiles in the middle and on the right are obtained with fixing the other quantities. (i) A comparison of densities (left) shows a fair agreement at the targets, while in the upstream SOL, SOLF1D gives 18% smaller density than SOLPS for the particle source in Fig. 3 and magnetic field from Fig. 1. (ii) The ion temperatures agree well everywhere on the flux tube, while the flat electron temperature predicted in SOLF1D is approximately 11% lower (case a). This trend remains even if we neglect viscous heating and energy exchange between electrons and ions (case b). (iii) Parallel ion velocities disagree by 35% (case a), however perfect match is obtained if the viscous flux is neglected (case b). Indeed, SOLPS takes into account an additional viscous flux driven by $\nabla_{\|} q$ which is not included in SOLF1D, see section 2.2. Apart from the viscous term, no other differences between the models have been identified. The disagreement in the density and temperature profiles is likely caused by the numerical discretization. In Figs. 5 and 7, the SOL is in the sheath-limited regime. This generally means that the particle transport, Eq. (9), is governed by the divergence of the flux, while in the high-recycling regime (Fig. 4), it is the recycling source that dominates the particle transport. The recycling source is calculated in EIRENE and it is treated in the same way as a net source in both codes. The origin of the disagreement in Fig. 7 therefore comes most likely from the way the flux divergence is calculated and how this term is discretized.

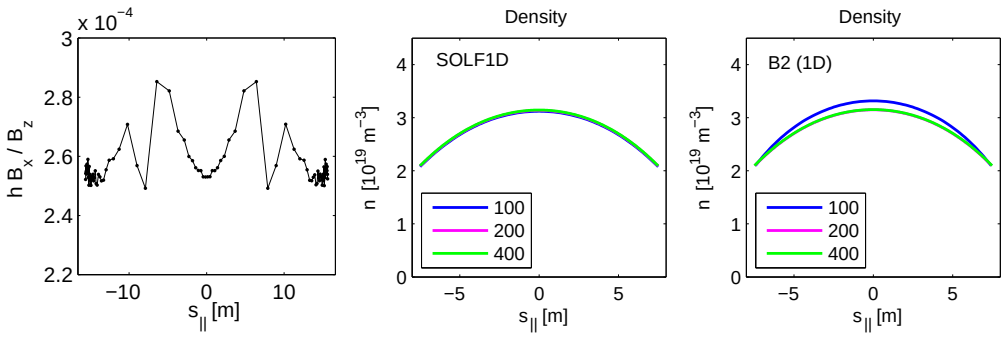

Figure 8. (i) Poloidal magnetic flux along the flux tube expressed as hB_x/B_z where h is the radial width of the flux tube (left). (ii) Test of spatial convergence of the SOLF1D continuity solver comparing solutions for different number of parallel grid points (middle). (iii) Spatial convergence of SOLPS (right).

As far as the discretization of the magnetic topology is concerned, it was shown in section 2.2 that the SOLPS equations are identical to the 1D equations solved in SOLF1D, if the condition of constant poloidal magnetic flux on the discretized flux surface is fulfilled. Fig. 8 (left) indicates that hB_x/B_z is constant in the divertor, however, approximately 12% oscillation above the average value occurs around X points. Similar level of discrepancy can be expected in the comparison of SOLPS/SOLF1D solutions. We can eliminate this numerical error by comparing SOLF1D with a 1D

version of SOLPS, assuming $B = \text{const}$ along the flux tube. Such comparison has been done previously in [12]. Identical solutions were obtained, see Fig. 8 (right), but only when the grid resolution in SOLPS was doubled from 100 to 200 grid points, with 6% difference between solutions on these two grids. Note that SOLPS typically runs on 100 poloidal cells, which is the case here. Fig. 9 compares solutions from SOLF1D and 1D SOLPS directly. Continuity and momentum solvers are identical and the electron temperatures now agree as well.

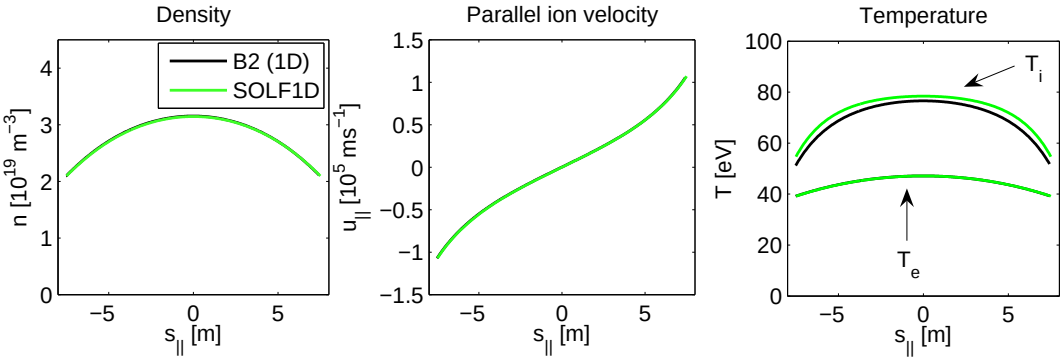

Figure 9. Comparison of solutions from SOLF1D and 1D version of SOLPS. The plasma density and parallel ion velocity (left and middle) are compared independently of the temperature solver with temperatures fixed to 60 eV. The electron and ion temperatures for a reduced model neglecting ion viscous heating are shown on the right.

Beside an inaccuracy in the discrete magnetic topology, Fig. 8 evidences an inaccuracy of the discretized equations which can be suppressed by refining the grid resolution. Different numerical schemes are used in the codes to treat the flux divergence and different methods to solve the discretized system of equations. The numerical technique of SOLF1D is described in appendix. SOLPS is based on the Patankar hybrid scheme and uses velocity-pressure coupling approach. While SOLF1D uses staggered grid, SOLPS stores $u_{\|}$ at the cell centres and uses an interpolation method to calculate fluxes at the cell faces. Indeed, differences (largest around the stagnation points) have been seen when switching from cell-faced to cell-centred version of SOLPS [david]. A numerical error can also result from the calculation of the flux divergence as the fluxes in and out of the flux tube have very close high values.

4. 1D effects of long-legged divertor

Power losses and particle sources in the SOL are affected by interaction of plasma with neutral species in the divertor. Power and particle SOL balance depends on the collisionality regime where the recycling at the targets competes with cross-field transport dominant in the upstream SOL. In Figs. 2 and 3, sources of particles, momentum and energy are shown on a flux tube in CD and SXD, separated as $S = S_{\perp} + S_{\text{coll}}$. Both conduction-limited and sheath-limited SOL display dominant

particle source at the targets due to ionization ($S^n_{\rm coll}$), compared to the cross-field transport source ($S^n_\perp$) which is strong around the stagnation point and X points. While the magnitude of $S^n_\perp$ does not change much in SXD, $S^n_{\rm coll}$ is factor of 3 larger. The energy source, on the other hand, is in both cases dominated by the radial transport, therefore enhanced electron cooling in SXD does not have a big impact on the power balance in the investigated regime (attached plasma). A detailed analysis of sources in the two topologies is given in Tab. 1, where integral sources along the flux tube (representing target fluxes) are calculated, clearly identifying the dominant terms that change the most with expanded divertor leg.

	CD	SXD	
$\int S^n \mathrm{d}s_\parallel$ [$\mathrm{m^{-2}s^{-1}}$]	5.0×10^{23}	1.8×10^{24}	3.5
$\int S^n_\perp \mathrm{d}s_\parallel$ [$\mathrm{m^{-2}s^{-1}}$]	-9.1×10^{21}	-3.5×10^{23}	38.5
$\int S^n_{\rm coll} \mathrm{d}s_\parallel$ [$\mathrm{m^{-2}s^{-1}}$]	5.1×10^{23}	2.1×10^{24}	4.2
$\int S^E \mathrm{d}s_\parallel$ [$\mathrm{kg\,s^{-3}}$]	4.6×10^{7}	6.9×10^{7}	1.5
$\int S^E_{\perp,\mathrm{e}} \mathrm{d}s_\parallel$ [$\mathrm{kg\,s^{-3}}$]	3.5×10^{7}	6.2×10^{7}	1.8
$\int S^E_{\perp,\mathrm{i}} \mathrm{d}s_\parallel$ [$\mathrm{kg\,s^{-3}}$]	1.7×10^{7}	1.7×10^{7}	1.0
$\int S^E_{\mathrm{coll,e}} \mathrm{d}s_\parallel$ [$\mathrm{kg\,s^{-3}}$]	-2.2×10^{6}	-8.7×10^{6}	4.0
$\int S^E_{\mathrm{coll,i}} \mathrm{d}s_\parallel$ [$\mathrm{kg\,s^{-3}}$]	-3.7×10^{6}	-2.3×10^{6}	0.6
$B_\mathrm{t} \int S^n/B \mathrm{d}s_\parallel$ [$\mathrm{m^{-2}s^{-1}}$]	5.0×10^{23}	1.6×10^{24}	3.2
$B_\mathrm{t} \int S^E/B \mathrm{d}s_\parallel$ [$\mathrm{kg\,s^{-3}}$]	8.0×10^{7}	4.7×10^{7}	0.6
B_t [T]	0.8	0.4	0.5
$Q_\parallel$ [$\mathrm{kg\,s^{-3}}$]	3.9×10^{7}	2.5×10^{7}	0.6
$Q_{\parallel,\mathrm{e}}$ [$\mathrm{kg\,s^{-3}}$]	2.0×10^{7}	1.7×10^{7}	0.9
$Q_{\parallel,\mathrm{i}}$ [$\mathrm{kg\,s^{-3}}$]	1.9×10^{7}	8.3×10^{6}	0.4
$\Gamma_\parallel$ [$\mathrm{m^{-2}s^{-1}}$]	2.2×10^{23}	8.3×10^{23}	3.7

Table 1. (top) Integral particle and energy sources on a flux tube of the CD and SXD configurations (a flux tube with maximum target energy load connecting outer targets). S^n is determined by $S^n_{\rm coll}$, which increases 4× with increased $L_\parallel$. Although $S^E_{\mathrm{coll,e}}$ changes 4×, S^E is mainly determined by $S^E_\perp$, which has weak dependence on $L_\parallel$, as well as $S^E_{\mathrm{coll,i}}$ which changes by factor of 0.6. Note that the flux tube on the outer side represents well the 2D picture, with the total change of particles by collisional processes in the entire grid volume by factor of 3, electron energy reduced by factor of 3 and the change in the ion energy of factor 0.6. (bottom) As a consequence of mass and energy conservation on the flux tube, the integral sources represent the target fluxes as $B \int S^n/B \mathrm{d}s_\parallel = 2\Gamma_\parallel$, $B \int S^E/B \mathrm{d}s_\parallel = 2Q_\parallel$.

As the particle and power balance on the flux tube in the outer SOL from Fig. 3 (Tab. 1) seems to represent well the balance in the entire outer SOL (see a comment in Tab. 1), we use the 1D approach to estimate the change in target parameters following from stretching the flux tube in the divertor. We start with the flux tube in the short divertor configuration (Fig. 5) which we expand in two directions (Fig. 10 left) labelled as (a) and (b). The magnetic field along the flux tube corresponding to these two

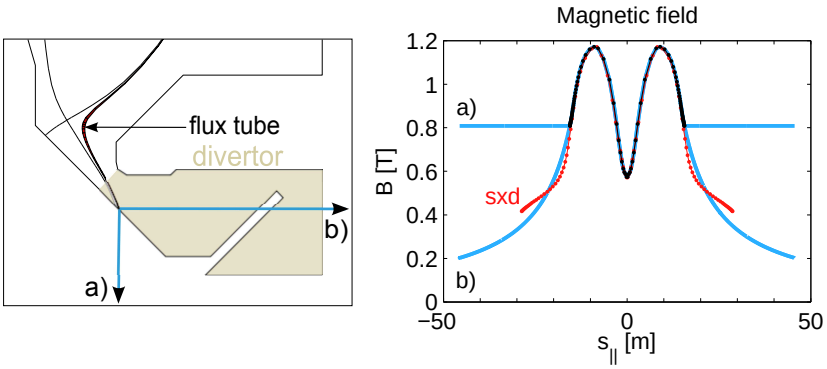

Figure 10. The scheme on the left shows a flux tube from SOLPS and different ways of stretching the divertor in 1D: (a) vertical stretching (magnetic field constant in the divertor), (b) radial stretching (magnetic field decreasing as $B \propto 1/R$). The graph on the right shows the magnetic field considered in the 1D code.

directions is plotted in Fig. 10 on the right (blue) and compared to the original CD case from Fig. 5 (black) and the SXD case from Fig. 4 (red). Particle and energy sources in the expanded divertor can not be self-consistently modelled in 1D, therefore they are approximated by a parametric dependence on the divertor length L_{div}, fitting the CD and SXD cases. The radial and recycling sources are treated separately. We assume that $S_\perp$, which is largest in the upstream SOL and around X points, does not change during stretching and it is zero in the newly created region. Further, we define a divertor region (Fig. 10 left – the region between the baffle and target) where we replace S_{coll} by its average value in this region $\overline{S}_{\mathrm{coll}}$. This does not change the target flux, but simplifies the treatment of sources during stretching the divertor leg. For the recycling source, we employ two methods: (1) While expanding the flux tube, we assume that $\int S_{\mathrm{coll}}$ is constant and S_{coll} in the divertor is replaced by its average value $\overline{S}_{\mathrm{coll}}$. (2) We assume that the uniformly distributed source in the divertor $\overline{S}_{\mathrm{coll}}$ is kept constant, i.e. the integrated source (or sink) $\int S_{\mathrm{coll}}$ grows with L_{div}. This approach partially incorporates 2D effects as we would expect the source due to recycling to be stronger with larger divertor volume.

The methods (1) and (2) are extreme cases with the SXD SOLPS simulation in between, as it can be shown by comparison of the 1D approximation of the sources with SOLPS results. The SOLPS simulations from Figs. 1-5 result in $\int S^E \mathrm{d}s_\parallel$ (integral along the flux tube) 1.5× larger in SXD than in CD and $\int S^n \mathrm{d}s_\parallel$ 3.5× larger (Tab. 1). The particle source S^n is dominated by recycling, while the energy source is dominated by radial transport (Fig. 3). This explains why $\int S^n$ grows with increasing L_{div} in contrast to $\int S^E$. As far as the recycling sources are concerned, the electron cooling in the divertor (negative source) is stronger by factor of 4 for SXD as well as the particle source due to ionization, and the ion recycling sources are comparable. The connection length increases 2×, and the divertor leg is approximately 8× longer (in parallel coordinate). The target energy flux in 1D with $\nabla_\parallel B$ effects is determined by

scan (1a)	$\mathbb{S}_{\rm div} = \mathbb{S}_0$	$B_{\rm div} = {\rm const}$
scan (1b)	$\mathbb{S}_{\rm div} = \mathbb{S}_0$	$B_{\rm div} \propto 1/R$
scan (2a)	$\mathbb{S}_{\rm div} = \mathbb{S}_0 L_{\rm div}/L_0$	$B_{\rm div} = {\rm const}$
scan (2b)	$\mathbb{S}_{\rm div} = \mathbb{S}_0 L_{\rm div}/L_0$	$B_{\rm div} \propto 1/R$
scan (3b-i)	$\mathbb{S}_{\rm div} = \mathbb{S}_0 (L_{\rm div}/L_0)^\gamma$	$B_{\rm div} \propto 1/R$
scan (3b-ii)	$\mathbb{S}_{\rm div} = \mathbb{S}_0 \gamma L_{\rm div}/L_0$	$B_{\rm div} \propto 1/R$

Table 2. The definition of cases considered in the analysis – the treatment of the sources and magnetic field in the expanded divertor. $\mathbb{S}_{\rm div}$ is the integral source in the divertor region $\mathbb{S}_{\rm div} = \int S_{\rm coll}$ of the length $L_{\rm div}$ and $\mathbb{S}_0$ is its reference value for the conventional divertor of the length L_0. The coefficients γ in the cases (3b-i) and (3b-ii) are chosen from fitting the SXD case.

$\int S^E/B{\rm d}s_\parallel$ (as $\int S^E/B{\rm d}s_\parallel = Q_\parallel/B_{\rm t}$) which is effectively the same for SXD with twice as long connection length $L_\parallel$ as for the short divertor (1.15× larger). The target energy flux is then approximately 1.6× smaller with the magnetic field at the target $B_{\rm t} \approx 0.4$ T compared to $B_{\rm t} \approx 0.8$ T in the short divertor. The recycling particle source is, however, much larger in SXD with $\int S^n/B{\rm d}s_\parallel$ being factor of 6 of the CD case. Note that the radial electron energy source increases by factor of 2, and because it dominates over the collisional cooling occurring in the divertor in both in CD and SXD, this effect should be taken into account. The increase of the radial source goes together with stronger parallel electron energy transport governed by conduction induced by steeper temperature gradients in SXD ($S^E_{\perp,{\rm e}} \approx S^E_{\parallel,{\rm e}} \approx -\kappa_{\rm e} k T_{\rm e}/L_{\nabla T_{\rm e}}$, $L^{\rm SXD}_{\nabla T_{\rm e}} < L^{\rm CD}_{\nabla T_{\rm e}}$).

The third method (3) defines an intermediate case. We assume that $\int S^n_{\rm coll}$ and $\int S^E_{\rm coll,e}$ are such functions of the divertor length $L_{\rm div}$, that both CD and SXD cases in Tab. 1 are matched. We keep $\int S^E_{\rm i}$ unchanged, but the amplitude of $S^E_{\perp,{\rm e}}$ increases with $L_{\rm div}$ as in SXD. This approximation is then used to predict target parameters for larger $L_{\rm div}$ beyond SXD. To interpolate between the CD and SXD cases, we assume a power dependence $\int S \propto L^\gamma_{\rm div}$ (i), and we also examine a linear dependence (ii). A summary of scans is given in Tab. 2.

Different treatment of sources in the flux tube, (1) versus (2) described above, and different directions of stretching the flux tube, (a) versus (b) from Fig. 10, give a combination of 4 scans, each shown in Fig. 11. In addition to these cases, an intermediate case (3) is shown, in which the sources fit the best the CD and SXD simulations. For the case (3), only radial stretching (b) is considered and 2 different fits, (i) and (ii), are assumed. The magenta case shown as (sxd) is the direct interpolation between CD and SXD, using the dependence (i). This case is close to the case (3b-i) where the divertor leg is stretched radially (Fig. 10 right in blue), with the difference of assuming directly the magnetic field and geometry of SXD (Fig. 10 right in red). The last point at $L_\parallel \approx 28$ m then corresponds to targets parameters found in SXD. (1a) In case of vertical stretching (no additional flux expansion in the divertor), the target quantities do not change and both the particle and energy fluxes remain the same with

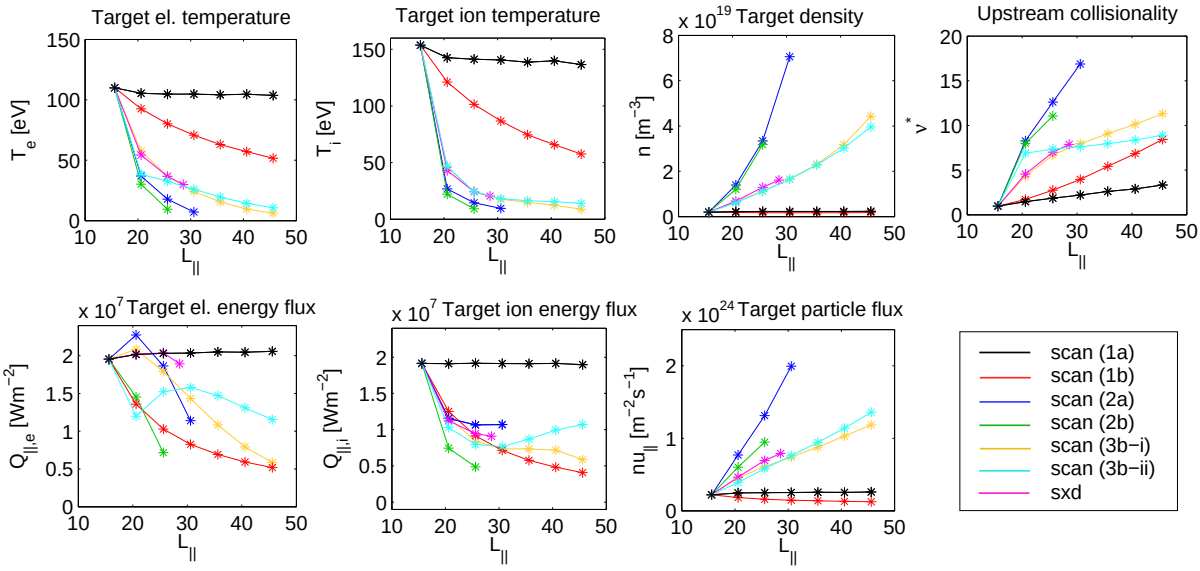

Figure 11. Parameters at the target calculated by SOLF1D as a function of the connection length, based on scans involving stretching of the divertor region as described in the text. (1a) constant integral sources in the flux tube (i.e. sources in the divertor are reduced proportionally to the increased divertor length) and constant magnetic field in the divertor (see Fig. 10 a). (1b) constant integral sources and varying magnetic field (Fig. 10 b). (2a) sources in the divertor multiplied by the divertor length and constant magnetic field in the divertor. (2b) sources in the divertor multiplied by the divertor length and varying magnetic field. (3b-i) sources in the divertor varied as $S \propto L_{\rm div}^{\alpha}$ with magnetic field as in case (b). (3b-ii) sources in the divertor varied as $S \propto L_{\rm div}$ with magnetic field as in case (b). (sxd) sources in the divertor varied as $S \propto L_{\rm div}$ with magnetic field as in SXD case.

increasing $L_{\rm div}$ (not surprising as $B_{\rm t}\int S^n/B{\rm d}s_{\|}$ and $B_{\rm t}\int S^E/B{\rm d}s_{\|}$ do not change with constant magnetic field in the divertor). (1b) Radial stretching (the magnetic field drops in the divertor as $B \propto 1/R$) leads already to a large reduction of temperatures and energy fluxes. This case shows the effect of magnetic flux expansion solely. (2a) With more recycling in the divertor, i.e. larger particle source and more cooling (the recycling sources scale with the divertor volume), the temperature drop is much steeper even without magnetic flux expansion (vertical stretching), however, we see less effect on the energy fluxes than flux expansion alone in the previous case. (2b) The most beneficial is the combination of both effects, which results in a substantial drop of both temperature and energy fluxes, increased density and particle flux, and higher collisionality. Cases (3b-i) and (3b-ii) represent an extrapolation from SXD to a divertor at larger radius, with different functions used to interpolate between CD and SXD. These cases lie between the limiting cases (1b) and (2b), both lead to a reduction of $T_{\rm e}$ approximately as $T_{\rm e} \propto L_{\|}^{-2.6}$. No further reduction of the energy fluxes is achieved before $L_{\|} \approx 45$ m compared to the reduction caused by magnetic flux expansion in case (1b). In spite of stronger volumetric power losses at larger $L_{\|}$ reducing the target energy flux, the parallel heat flux governed mainly by the source due to cross-field transport is

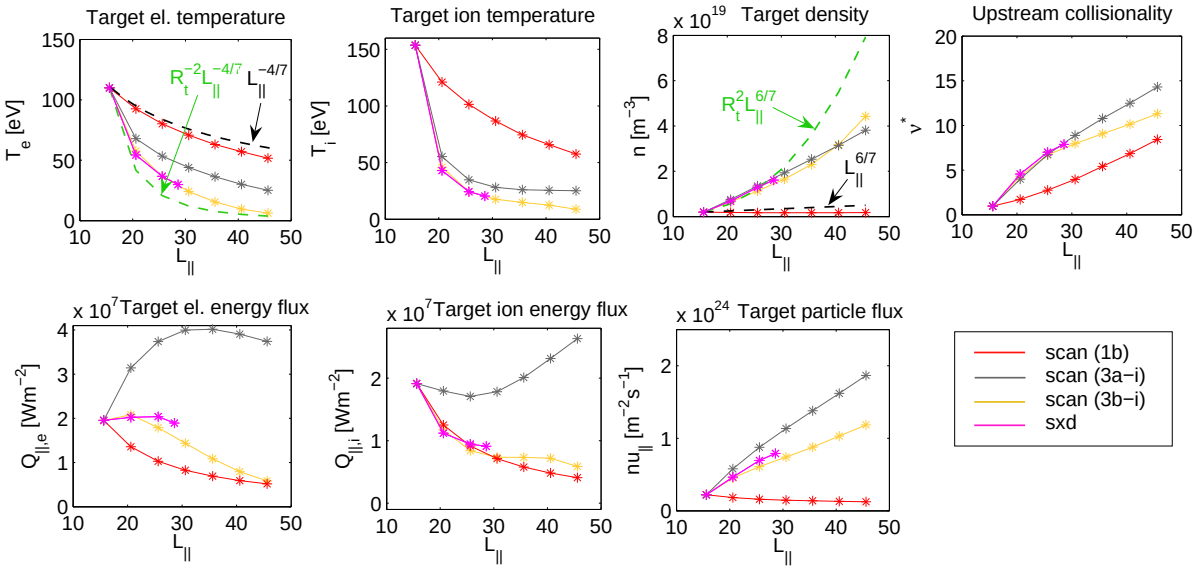

Figure 12. Parameters at the target calculated by SOLF1D compared to the two-point model. (1b) the effect of magnetic flux expansion solely as in Fig. 11, i.e. the magnetic field varies as $B \propto 1/R$ and the sources due to recycling and collisions have constant integral. (3a-i) constant magnetic field in the divertor, sources in the divertor vary as $S \propto L_{\rm div}^{\alpha}$ and match the CD and SXD cases at $L_{||} \approx 15$ m and $L_{||} \approx 28$ m. (3b-i) as in Fig. 11, i.e. the magnetic field in the divertor goes as $B \propto 1/R$, sources in the divertor go as $S \propto L_{\rm div}^{\alpha}$. (sxd) as in Fig. 11, the magnetic field and sources change as in SXD, plasma parameters at $L_{||} \approx 15$ m coincide with CD values and at $L_{||} \approx 28$ m with SXD values. For comparison, the two-point model without/with $R_{\rm t}$ dependence is shown in black/green.

enhanced (stronger $\nabla_{\|} T_{\rm e}$ at increased $L_{\|}$). These two effects compete and the collisional cooling starts to dominate only at large $L_{\|}$ in this density regime. Note that different extrapolations (i) or (ii) lead to similar n and T in the divertor, while the prediction of $Q_{\|}$ for large $L_{\|}$ is more sensitive to the actual dependence of the collisional source on $L_{\|}$.

In Fig. 12, the reduction of the electron temperature and the increase of the density at the target is compared with a two-point model prediction. As in Fig. 11, a scan with SXD parameters is shown (magenta) with an extrapolation extending the divertor even further radially (3b-i, yellow), together with a scan showing the effect of magnetic flux expansion solely (1b, red). In addition, a scan assuming vertical stretching instead of the radial one is plotted (3a-i, grey). The case (3a-i), where $T_{\rm e}$ falls as $T_{\rm e} \propto L_{\|}^{-1.3}$, shows steeper temperature drop than predicted by the two-point model ($T_{\rm e} \propto L_{\|}^{-4/7}$ and $n_{\rm e} \propto L_{\|}^{6/7}$). The cases (sxd) and (3b-i), on the contrary, show weaker dependence than a modified two-point model taking into account the dependence on the target radius $R_{\rm t}$ ($T_{\rm e} \propto R_{\rm t}^{-2} L_{\|}^{-4/7}$ and $n_{\rm e} \propto R_{\rm t}^{2} L_{\|}^{6/7}$).

Fig. 13 shows parallel profiles for the scans from Fig. 11. In the first row (1a), the SOL is in the sheath-limited regime and no reduction of temperatures is observed. In the second row (1b), the temperature is reduced through magnetic flux expansion and

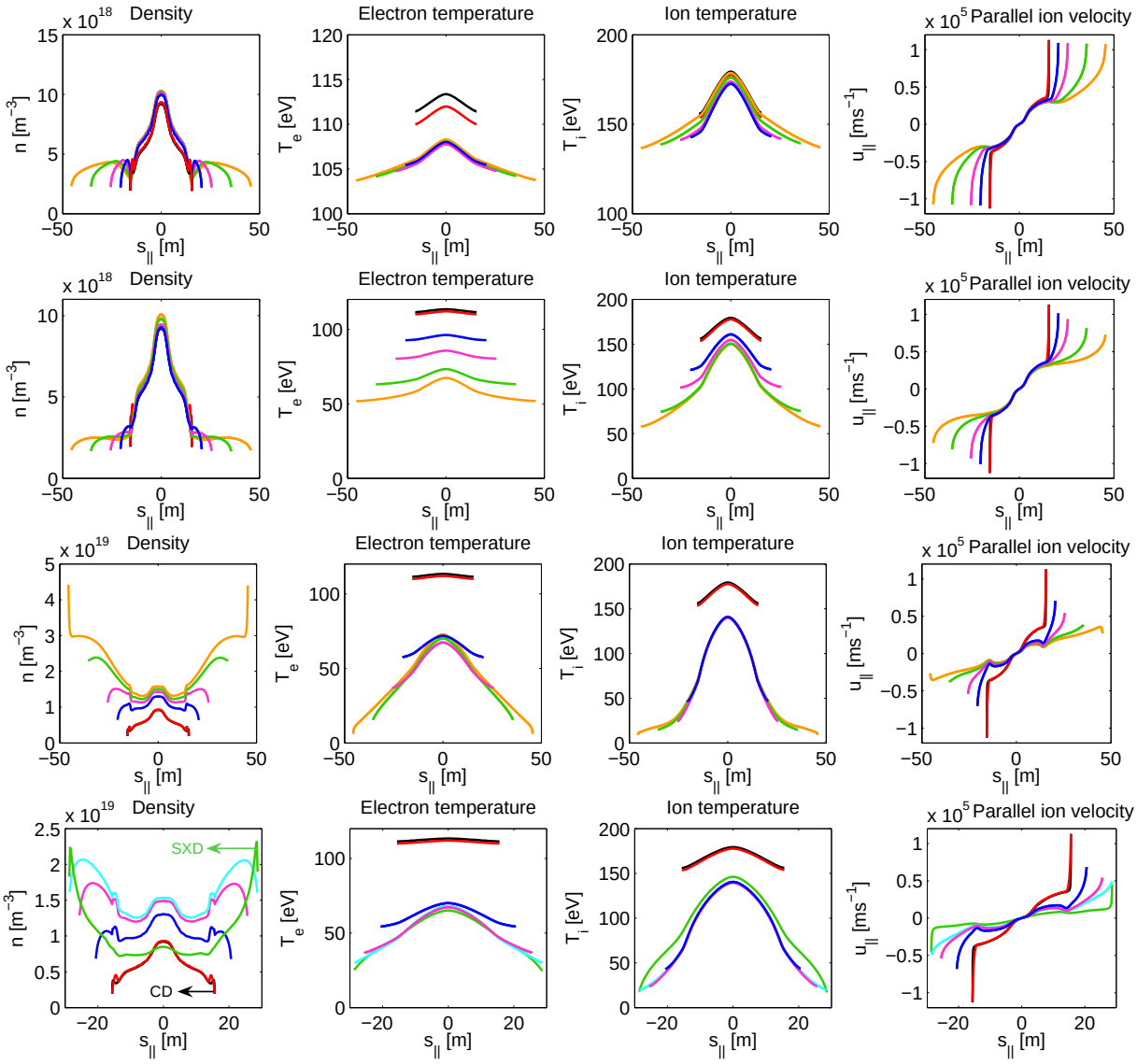

Figure 13. Parallel profiles of plasma quantities on a flux tube between upper and lower outer targets for an expanded divertor leg: (i) Case (1a) from Fig. 11. (ii) Case (1b) from Fig. 11 (increasing flux expansion). (iii) Case (3b-i) from Fig. 11 (increasing flux expansion and strength of recycling sources). In black, profiles for the CD geometry (as in Fig. 5). In red, a solution for the CD geometry with recycling sources at the target replaced uniformly by the average value in the divertor. In blue, magenta, green and orange, solutions for the expanded divertor. (iv) Case (sxd) from Fig. 11 (changing flux expansion and strength of recycling sources as in SXD). In black, profiles for the CD geometry (from Fig. 5). In blue, magenta and cyan, profiles for the expanded divertor. The last profile at $L_{||} = 28$ m coincides at the targets with the solution for the SXD geometry (from Fig. 4) shown in green.

the temperature profiles remain flat. In the third row (3b-i), the conduction-limited SOL is accessed by increased plasma-neutral cooling in the divertor accompanied by a drop of the plasma temperature at the target and an increase of the density. The last case displays profiles for the case (sxd) from Fig. 11 where target parameters for

$L_\parallel \approx 28$ m coincide with the previous solution for SXD in Fig. 4.

5. Conclusions

In order to use the SOLF1D code to predict conditions at the target for a long-legged divertor, the code has been first benchmarked with SOLPS. The comparison shows perfect agreement for the collisional SOL and satisfactory agreement for the sheath-limited SOL, with discrepancies partly caused by numerical errors related to the discretization of SOLPS equations on a 2D grid and partly by inaccurate conservation of the poloidal magnetic flux on the flux surface, once discretized on the grid. These discrepancies are, however, not large (15%) and might reduce by higher resolution of the 2D grid.

Based on the successful benchmark of SOLF1D with SOLPS for two divertor geometries (conventional and Super-X divertor), an extrapolation to larger $L_\parallel$ is carried out. The effect of magnetic flux expansion on the reduction of target temperature and energy flux is separated from the effect of power loss due to atomic processes by stretching the divertor leg in either radial ($B \propto 1/R$) or vertical (no additional flux expansion) direction. Between the conventional divertor geometry ($L_\parallel \approx 15$ m) and SXD ($L_\parallel \approx 28$ m), T_e in front of the target drops from 111 eV to 25 eV and for $L_\parallel \approx 45$ m (the divertor leg extended in radial direction), T_e is further reduced to 6 eV. The temperature is reduced equally by magnetic flux expansion and plasma-neutral collision effects in this collisionality regime ($n_\mathrm{sep} \approx 9\times10^{18}$ m^{-3}, $P_\mathrm{inp} \approx 1.7$ MW) and the T_e drop in SXD is slower than predicted by the two-point model. $Q_\parallel$ drops from 38.6 MWm^{-2} (CD) to 25.1 MWm^{-2} (SXD) under attached divertor conditions and for $L_\parallel \approx 45$ m, an additional drop to 11.7 MWm^{-2} is predicted. The dominant effect responsible for reducing $Q_\parallel$ at the target is magnetic flux expansion, while volumetric power loss in the divertor (smaller compared to the energy source due to upstream cross-field transport) starts to play a role at large $L_\parallel$ ($L_\parallel \approx 45$ m), unless the density (radiation) is increased.

Acknowledgments

This work was supported by EURATOM and carried out within the framework of the European Fusion Development Agreement. The views and opinions expressed herein do not necessarily reflect those of the European Commission. The CCFE authors were funded by the RCUK Energy Programme under grant EP/G003955.

Appendix – SOLF1D model

5.1. Generalized equations

The model is based on the following equations for the plasma density n, parallel ion velocity $u_\parallel$ and electron and ion temperatures T_e and T_i

$$\frac{\partial n}{\partial t} + B\frac{\partial}{\partial s}\left(\frac{nu_\parallel}{B}\right) = S^n, \tag{13}$$

$$\frac{\partial}{\partial t}(m_\mathrm{i} n u_\parallel) + B\frac{\partial}{\partial s}\left(\frac{m_\mathrm{i} n u_\parallel^2}{B}\right) + B^{\frac{3}{2}}\frac{\partial}{\partial s}\left(B^{-\frac{3}{2}}\delta p_\mathrm{i}\right) = -\frac{\partial}{\partial s}(p_\mathrm{e}+p_\mathrm{i}) + m_\mathrm{i} S^u, \tag{14}$$

$$\frac{\partial}{\partial t}\left(\frac{3}{2}nkT_\mathrm{e}\right) + B\frac{\partial}{\partial s}\left[\frac{1}{B}\left(\frac{5}{2}nkT_\mathrm{e}u_\parallel + q_{\parallel,\mathrm{e}}\right)\right] = u_\parallel\frac{\partial p_\mathrm{e}}{\partial s} + Q_\mathrm{e} + S_\mathrm{e}^E \tag{15}$$

$$\frac{\partial}{\partial t}\left(\frac{3}{2}nkT_\mathrm{i} + \frac{1}{2}m_\mathrm{i} n u_\parallel^2\right) + B\frac{\partial}{\partial s}\left[\frac{1}{B}\left(\frac{5}{2}nkT_\mathrm{i}u_\parallel + \frac{1}{2}m_\mathrm{i} n u_\parallel^3 + q_{\parallel,\mathrm{i}} + u_\parallel\delta p_\mathrm{i}\right)\right] = \tag{16}$$

$$-u_\parallel\frac{\partial p_\mathrm{e}}{\partial s} + Q_\mathrm{i} + S_\mathrm{i}^E$$

assuming quasineutrality ($n_\mathrm{e} = n_\mathrm{i}$), no net parallel current ($j_\parallel = 0$) and ambipolarity ($u_{\parallel,\mathrm{e}} = u_{\parallel,\mathrm{i}}$). We further assume the generalized Ohm's law for electron momentum $enE_\parallel = -\partial p_\mathrm{e}/\partial s + R_{\parallel,\mathrm{e}}$ which leads to the cancellation of terms with thermal forces $R_{\parallel,\mathrm{e}} = -R_{\parallel,\mathrm{i}}$ and parallel electric field $E_\parallel$ in the momentum and energy equations and the substitution by $\partial p_\mathrm{e}/\partial s$ term, see Eqs. 1-4.

5.2. Relation to Braginskii model

The set of equations is consistent with Braginskii equations, see [3]. The divergence of the velocity vector $\mathbf{u}$ in the three-dimensional continuity equation of Braginskii (or analogically the energy flux vector in the energy equation) is replaced by

$$\nabla\cdot\mathbf{u} \rightarrow \frac{\partial u_\parallel}{\partial s} - \frac{u_\parallel}{B}\frac{\partial B}{\partial s} = B\frac{\partial}{\partial s}\left(\frac{u_\parallel}{B}\right), \tag{17}$$

leading to Eq. (13). We obtain the new operator in (17) by expanding the velocity as $\mathbf{u} = u_\parallel\mathbf{b} + \mathbf{u}_\perp$ and using $\nabla\cdot\mathbf{B} = 0$ where $\mathbf{b} = \mathbf{B}/B$. The component perpendicular to the magnetic field will appear as a source term on the right-hand side of the one-dimensional equation.

The momentum equation, Eq. (14), is the parallel component of Braginskii momentum equation. Braginskii viscosity tensor $\pi \equiv \mathbf{P} - p\mathbf{I}$ yields

$$\pi = \delta p_\mathrm{i}\left(\frac{3}{2}\mathbf{bb} - \frac{1}{2}\mathbf{I}\right), \tag{18}$$

if following definitions are used $\mathbf{P} \equiv p_\parallel\mathbf{bb} + p_\perp(\mathbf{I}-\mathbf{bb})$, $p \equiv (p_\parallel + 2p_\perp)/3$ and $\delta p_\mathrm{i} \equiv p_\parallel - p$. The parallel component of the viscous term in Braginskii momentum equation is then equivalent to

$$\mathbf{b}\cdot\nabla\cdot\pi = \frac{\partial\delta p_\mathrm{i}}{\partial s} - \frac{3}{2}\frac{\delta p_\mathrm{i}}{B}\frac{\partial B}{\partial s} = B^{\frac{3}{2}}\frac{\partial}{\partial s}\left(B^{-\frac{3}{2}}\delta p_\mathrm{i}\right). \tag{19}$$

In order to complete the description of the model, a closure of the equations is required (i.e. expressions for the viscous momentum flux δp_i and the thermal heat fluxes $q_{\parallel,\mathrm{e}}$ and $q_{\parallel,\mathrm{i}}$) and all transport coefficients and source terms arising due to plasma-neutral interactions must be defined.

5.3. Parallel ion viscosity

The parallel viscous flux is written as

$$\delta p_\mathrm{i} \approx -\eta_\parallel \left(\frac{\partial u_\parallel}{\partial s} + \frac{u_\parallel}{2B}\frac{\partial B}{\partial s} \right) = -\eta_\parallel B^{-\frac{1}{2}} \frac{\partial}{\partial s}\left(B^{\frac{1}{2}} u_\parallel \right). \tag{20}$$

Note that the form of Eq. (20) is again consistent with Braginskii parallel viscous momentum flux, if we replace $\nabla \cdot \mathbf{u}$ by Eq. (17) in individual components of Braginskii viscosity tensor. We can use the classical Braginskii parallel viscosity

$$\eta_\parallel = \eta_\mathrm{cl} = 0.96 n k T_\mathrm{i} \tau_\mathrm{i} \tag{21}$$

or employ viscous flux limiters in order to satisfy all collisionality regimes. The collision time τ_i is defined as

$$\tau_\mathrm{i} = \frac{3\sqrt{m_\mathrm{i}}(kT_\mathrm{i})^{\frac{3}{2}}}{4\sqrt{\pi} n \lambda e^4} = 2.09 \times 10^{13} \frac{T_\mathrm{i}^{\frac{3}{2}}}{n\lambda}\sqrt{\frac{m_\mathrm{i}}{m_\mathrm{p}}}\mathrm{sec} \tag{22}$$

in SI units and Boltzmann constant is $k = 1.6 \times 10^{-19}$ J/eV [7]. The Coulomb logarithm λ is generally a function of the density and temperature, see e.g. [8] or [9].

If we follow the derivation of the parallel and perpendicular pressure equations as done for example in [3] or [5], we can obtain more general equation for the parallel viscous flux δp_i which defines a parallel viscosity limiter through

$$\eta_\parallel = \frac{\eta_\mathrm{cl}}{1+\Omega_\eta}, \quad \Omega_\eta = \frac{\eta_\mathrm{cl}\nabla_\parallel u_\parallel}{\frac{4}{7} n k T_\mathrm{i}} - \frac{\eta_\mathrm{cl} u_\parallel \nabla_\parallel B}{B n k T_\mathrm{i}}. \tag{23}$$

Eq. (23) reduces to the expression (21) in the limit of high collisionality. In widely used 2D transport codes such as SOLPS or EDGE2D, only the $\nabla_\parallel u_\parallel$ term is taken into account, with the ion viscous flux limiter as an optional parameters in the code, but typically $\beta_u = 0.5$ ($\approx 4/7$) being a good choice in steady-state inter-ELM modelling of the low-recycling SOL.

5.4. Parallel heat conductivity

From higher-order moment equations, approximate expressions for the heat flux can be obtained. We calculate the heat flux using classical Spitzer-Härm heat conductivities

$$q_{\parallel,\mathrm{e}} = -\kappa_e \frac{\partial}{\partial s}(kT_\mathrm{e}), \quad \kappa_\mathrm{e} = \kappa_{\mathrm{cl,e}} = 3.2\frac{n k T_\mathrm{e} \tau_\mathrm{e}}{m_\mathrm{e}}, \tag{24}$$

$$q_{\parallel,\mathrm{i}} = -\kappa_i \frac{\partial}{\partial s}(kT_\mathrm{i}), \quad \kappa_\mathrm{i} = \kappa_{\mathrm{cl,i}} = 3.9\frac{n k T_\mathrm{i} \tau_\mathrm{i}}{m_\mathrm{i}}, \tag{25}$$

$$\tag{26}$$

and define the electron collision time as

$$\tau_{\rm e} = \frac{3\sqrt{m_{\rm e}}(kT_{\rm e})^{\frac{3}{2}}}{4\sqrt{2\pi}n\lambda e^4} = 3.44\times10^{11}\frac{T_{\rm e}^{\frac{3}{2}}}{n\lambda}{\rm sec}. \tag{27}$$

Kinetic corrections in the form of heat flux limiters can be used. SOLF1D allows to modify the thermal heat flux both for the electrons and ions as

$$q_\parallel = \left(\frac{1}{q_{\parallel,\rm lim}} + \frac{1}{q_{\parallel,\rm cl}}\right)^{-1} \tag{28}$$

which limits the heat flux to a maximum acceptable value $q_{\parallel,\rm lim} = \alpha n v^{\rm th} kT$, where $v^{\rm th}$ is the thermal speed, and imposes a limit for the heat conductivity which would otherwise diverge for large temperatures. From Eq. (28), a corrected expression for the heat conductivity can be formulated as

$$\kappa = \frac{\kappa_{\rm cl}}{1+\Omega_\kappa}, \quad \Omega_\kappa = \frac{\kappa_{\rm cl}\nabla_\parallel T}{\alpha n v^{\rm th} T}. \tag{29}$$

The electron and ion heat flux limiters $\alpha_{\rm e}$ and $\alpha_{\rm i}$ are again optional parameters of the model. As a result of kinetic studies, values of the heat flux limiters are observed in the range $0.03 \le \alpha \le 0.6$ with poloidally averaged values $\alpha \approx 0.15 \pm 0.05$ (depending on the collisionality) and for the viscosity limiter it is $\beta \approx 0.5 \pm 0.1$ [14]. At high collisionalities, no limiting is required and some authors mention a heat flux enhancement contrary to limiting [15]. The limiters strongly vary in time, e.g. during ELMs or turbulent transport, by several orders of magnitude [14] and the latest comparison of SOLF1D with the kinetic code BIT1 has shown that assuming constant heat flux limiters during the ELM crash is not adequate [16].

5.5. Model of neutrals

Atomic species are treated as a fluid and their transport is described by 1D continuity and momentum transfer equations

$$\frac{\partial n_0}{\partial t} + \frac{\partial}{\partial s}\left(n_0 u_0\right) = S_0^n, \tag{30}$$

$$\frac{\partial}{\partial t}\left(m_0 n_0 u_0\right) + \frac{\partial}{\partial s}\left(m_0 n_0 u_0^2\right) = -\frac{\partial p_0}{\partial s} + m_0 S_0^u \tag{31}$$

with the density and momentum sources/sinks S_0^n balanced by corresponding ionic sinks/sources in the plasma fluid equations. The closure is made using an assumption about the energy of neutrals. Neutral species are assumed to thermally equilibrate with ions due to dominant charge-exchange processes and therefore considered to have the temperature locally equal to the ion temperature $T_0 = T_{\rm i}$ everywhere in the SOL.

The 1D model of neutrals provides a simple way to incorporate the main aspects of the SOL for different collisionalities and to describe high-recycling conditions. While the 1D description is reasonable for plasma, 2D modelling of neutrals would be more appropriate, especially if the ionization mean free path is long enough for neutrals to propagate deeper in the SOL. In such case, 1D model can lead to overestimation of

neutral concentration on the flux tube or eventually result in instable solutions. 2D codes such as SOLPS are usually coupled with Monte Carlo EIRENE and there has been an evidence that the kinetic treatment is certainly required for precise quantitative calculations (see e.g. [10] and [11]). Both plasma and neutral models in SOLF1D are currently being benchmarked with PIC simulations performed with BIT1 code for different collisionalities and results will be published shortly.

5.6. Collision and source terms

The energy exchange between electron and ions due to collisions is described as

$$Q_{\mathrm{i}} = -Q_{\mathrm{e}} = \frac{3m_{\mathrm{e}}}{m_{\mathrm{i}}}\frac{nk}{\tau_{\mathrm{e}}}(T_{\mathrm{e}} - T_{\mathrm{i}}). \tag{32}$$

The sources S^n, S^u, S^E_{e} and S^E_{i} in Eqs. (13)-(16) comprise cross-field sources of plasma, momentum (here neglected) and energy and collision terms (the interaction of plasma with neutrals) describing changes of the mass, momentum and energy due to processes of ionization, charge exchange, excitation and recombination. They are defined as

$$S^n = n_0 n\langle\sigma v\rangle_{\mathrm{ION}} - n^2\langle\sigma v\rangle_{\mathrm{REC}} + S^n_{\perp}, \tag{33}$$

$$S^u = n_0 n u_0\langle\sigma v\rangle_{\mathrm{ION}} + n_0 n(u_0 - u_{\parallel})\langle\sigma v\rangle_{\mathrm{CX}} - n^2 u_{\parallel}\langle\sigma v\rangle_{\mathrm{REC}}, \tag{34}$$

$$S^E_{\mathrm{e}} = -n_0 n\langle\sigma v\rangle_{\mathrm{ION}} k I_{\mathrm{H}} - n_0 n k Q_{\mathrm{H}} + S^E_{\perp,e}, \tag{35}$$

$$\begin{aligned} S^E_{\mathrm{i}} &= n_0 n\langle\sigma v\rangle_{\mathrm{ION}}\left[\frac{3}{2}kT_0 + \frac{1}{2}m_0 u_0^2\right] \\ &+ n_0 n\langle\sigma v\rangle_{\mathrm{CX}}\left[\frac{3}{2}k(T_0 - T_{\mathrm{i}}) + \frac{1}{2}m_0(u_0^2 - u_{\parallel}^2)\right] \\ &- n^2\langle\sigma v\rangle_{\mathrm{REC}}\left[\frac{3}{2}kT_{\mathrm{i}} + \frac{1}{2}m_0 u_{\parallel}^2\right] + S^E_{\perp,i}. \end{aligned} \tag{36}$$

I_{H} is the ionization potential ($I_{\mathrm{H}} = 13.6$ eV for hydrogen ions), Q_{H} is the cooling rate due to excitation and $\langle\sigma v\rangle_{\mathrm{ION}}$, $\langle\sigma v\rangle_{\mathrm{CX}}$ and $\langle\sigma v\rangle_{\mathrm{REC}}$ are collision rates for ionization, charge exchange and recombination which are, in general, functions of the density and temperature, see Fig. 14.

5.7. Numerical solution

The equations in SOLF1D are solved numerically in variables n, $u_{\parallel}$, T_{e} and T_{i}, i.e. equations (13)–(16) are modified as

$$\frac{\partial n}{\partial t} + B\frac{\partial}{\partial s}\left(B^{-1} n u_{\parallel}\right) = S^n, \tag{37}$$

$$\begin{aligned} m_{\mathrm{i}} n\frac{\partial u_{\parallel}}{\partial t} + \frac{1}{2}m_{\mathrm{i}} n\frac{\partial}{\partial s}(u_{\parallel}^2) - B^{\frac{3}{2}}\frac{\partial}{\partial s}\left[B^{-2}\eta_{\parallel}\frac{\partial}{\partial s}\left(B^{\frac{1}{2}}u_{\parallel}\right)\right] = \\ -\frac{\partial}{\partial s}(p_{\mathrm{e}} + p_{\mathrm{i}}) + m_{\mathrm{i}} S^u - m_{\mathrm{i}} u_{\parallel} S^n, \end{aligned} \tag{38}$$

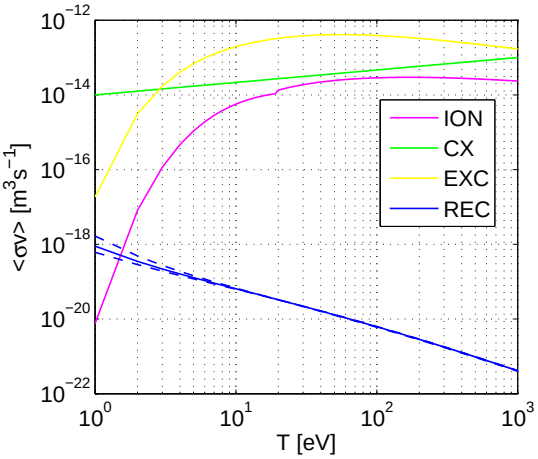

Figure 14. Collision rates used in the SOLF1D code. The recombination rate is displayed for densities $n = 1 \times 10^{18}$ m^{-3}, $n = 1 \times 10^{19}$ m^{-3} and $n = 1 \times 10^{20}$ m^{-3}.

$$\frac{3}{2}nk\frac{\partial T_\mathrm{e}}{\partial t} + \frac{3}{2}nk\frac{\partial}{\partial s}(T_\mathrm{e}u_\parallel) - B\frac{\partial}{\partial s}\left[B^{-1}\kappa_\mathrm{e}\frac{\partial}{\partial s}(kT_\mathrm{e})\right] = \frac{1}{2}nkT_\mathrm{e}\frac{\partial u_\parallel}{\partial s} - \frac{3}{2}kT_\mathrm{e}S^n + Q_\mathrm{e} + S_\mathrm{e}^E + \frac{nkT_\mathrm{e}u_\parallel}{B}\frac{\partial B}{\partial s}, \tag{39}$$

$$\frac{3}{2}nk\frac{\partial T_\mathrm{i}}{\partial t} + \frac{3}{2}nk\frac{\partial}{\partial s}(T_\mathrm{i}u_\parallel) - B\frac{\partial}{\partial s}\left[B^{-1}\kappa_\mathrm{i}\frac{\partial}{\partial s}(kT_\mathrm{i})\right] = \frac{1}{2}nkT_\mathrm{i}\frac{\partial u_\parallel}{\partial s} + \eta_\parallel\left(\frac{\partial u_\parallel}{\partial s}\right)^2 - \frac{3}{2}kT_\mathrm{i}S^n + \frac{1}{2}m_\mathrm{i}u_\parallel^2 S^n - m_\mathrm{i}u_\parallel S^u + Q_\mathrm{i} + S_\mathrm{i}^E + \frac{nkT_\mathrm{i}u_\parallel}{B}\frac{\partial B}{\partial s} + \frac{\eta_\parallel u_\parallel}{B}\frac{\partial B}{\partial s}\frac{\partial u_\parallel}{\partial s} + \frac{\eta_\parallel u_\parallel^2}{4B^2}\left(\frac{\partial B}{\partial s}\right)^2, \tag{40}$$

and solved in a similar form

$$a\frac{\partial f}{\partial t} + b\frac{\partial}{\partial s}(fv) + c\frac{\partial}{\partial s}\left[d\frac{\partial}{\partial s}(ef)\right] = S_1 + fS_2. \tag{41}$$

The system of nonlinear equations is solved by an algorithm based on the finite difference method. The equations are discretized on a non-uniform staggered grid using traditional numerical schemes and solved by a mixed explicit/implicit time integration. We use an exponential grid with refined spacing in the boundary regions where large gradients of plasma quantities can occur in high-recycling or detached regimes. The convective terms of the fluid equations are converted to finite difference expressions by the second-order upwind scheme and the diffusive terms are discretized by the Crank-Nicholson scheme. The time stepping is based on the second-order splitting method (see e.g. [17]). Nonlinear terms are treated explicitly, while linear terms are updated to a new time level implicitly. Resulting systems of linear equations are solved by the Progonka and Matrix Progonka methods described in [12].

5.8. Boundary conditions

At both ends of the computational region (target plates), boundary conditions are applied (see Tab. 3), including Bohm criterion for the parallel ion velocity (Dirichlet boundary condition) and standard expressions for the sheath energy fluxes using constant sheath energy transmission factors (the condition for the flux is linearized and translated into Newton boundary condition for the temperature). A pumping at the target and neutral recycling is included using the recycling coefficient and recycled neutrals are assumed to propagate from the targets with the thermal speed at the temperature $T_0 = T_\mathrm{i}$ (neutrals leaving the wall are assumed to equilibrate fast with plasma ions due to charge exchange). The density is extrapolated from the neighbouring points to the boundary.

quantity	**boundary condition**
n	extrapolation
$u_\parallel$	$u_\parallel = c_\mathrm{s} \equiv \sqrt{\frac{k(T_\mathrm{e}+T_\mathrm{i})}{m_\mathrm{i}}}$
T_e	$Q_{\parallel,\mathrm{e}} = \delta_\mathrm{e} n k T_\mathrm{e} c_\mathrm{s}$
T_i	$Q_{\parallel,\mathrm{i}} = \delta_\mathrm{i} n k T_\mathrm{i} c_\mathrm{s}$
n_0	$\Gamma_0 = -R\Gamma_\parallel$
u_0	$u_0 = v^\mathrm{th} \equiv \sqrt{\frac{kT_0}{m_0}}$

Table 3. Boundary conditions of the SOLF1D model.

References

[1] Fishpool G et al 2012 *20th PSI conference, Aachen, Germany* P1-11 (to be submitted to *J. Nucl. Mater.*)
[2] Havlíčková E et al 2011 *Plasma Phys. Control. Fusion* **53** 065004
[3] Zawaideh E et al 1986 *Phys. Fluids* **29** (2) 463
[4] Zawaideh E et al 1988 *Phys. Fluids* **31** (11) 3280
[5] Fundamenski W 2005 *Plasma Phys. Control. Fusion* **47** R163
[6] Schneider R et al 2006 *Contrib. Plasma Phys.* **46** 3
[7] NRL plasma formulary URL http://wwwppd.nrl.navy.mil/nrlformulary/index.html
[8] Wesson J 2004 *Tokamaks* (New York: Oxford University Press)
[9] Stangeby P C 2000 *The Plasma Boundary of Magnetic Fusion Devices* (Bristol: Institute of Publishing)
[10] Coster D P et al 2004 *Physica Scripta* **T108** 7
[11] Havlíčková E et al (to be submitted)
[12] Havlíčková E 2009 *PhD Thesis* Charles University, Prague
[13] Havlíčková E et al 2012 *20th PSI conference, Aachen, Germany* P1-52 (to be submitted to *J. Nucl. Mater.*)
[14] Tskhakaya D et al 2008 *Contrib. Plasma Phys.* **48** 89
[15] Chankin A V and Coster D P 2008 *18th PSI conference, Toledo, Spain*
[16] Havlíčková E et al 2012 *Plasma Phys. Control. Fusion* **54** 045002
[17] Karniadakis G E et al 1991 *J. Comput. Phys.* **97** 414